Flow characteristics in vertical circular pipes with the square top end under flooding conditions

Takaki, Toshiya

Goda, Raito

Hayashi, Kosuke

Murase, Michio

Tomiyama, Akio

(Citation)
Nuclear Engineering and Design,371:110951

(Issue Date)
2021-01

(Resource Type)
journal article

(Version)
Accepted Manuscript

Flow characteristics in vertical circular pipes with the square top end under flooding conditions

Toshiya Takaki,[a,b]* Raito Goda,[b] Kosuke Hayashi,[b] Michio Murase,[a] Akio Tomiyama [b]

[a] *Institute of Nuclear Safety System, Inc., 64 Sata, Mihama-cho, Mikata-gun, Fukui 919-1205, Japan*

[b] *Graduate School of Engineering, Kobe University, 1-1 Rokkodai, Nada-ku, Kobe-shi, Hyogo 657-8501, Japan*

* Institute of Nuclear Safety System, Inc., 64 Sata, Mihama-cho, Mikata-gun, Fukui 919-1205, Japan

Tel. +81-770-37-9100, Fax. +81-770-37-2009, E-mail: takaki.toshiya@inss.co.jp

Credit author statement:
No potential conflict of interest was reported by the authors.

Declaration of interest statement:
This study was supported by a private company that has agreed to publishing of the results.

Highlights

- Void fractions in a vertical pipe under flooding at its square top end were measured.
- CCFL was expressed by Wallis and Kutateladze parameters for 20 and 40 mm diameter, respectively.
- Wall friction and interfacial friction factors under flooding at the square top end were evaluated.
- A correlation for the wall friction factor under flooding at the square top end was proposed.

Flow characteristics in vertical circular pipes with the square top end under flooding conditions

Toshiya TAKAKI, Raito GODA, Kosuke HAYASHI, Michio MURASE, Akio TOMIYAMA

Abstract

Previously, we evaluated flow characteristics in a vertical pipe of diameter D = 20 mm under flooding conditions. Now, we have measured the void fraction α, pressure gradient dP/dz and countercurrent flow limitation (CCFL) characteristics in a vertical pipe of D = 40 mm with the square (i.e. sharp-edged without curvature) top end, and air and water to evaluate the film thickness δ, the wall friction factor f_w and the interfacial friction factor f_i. The comparison of flow characteristics between pipes of D = 20 and 40 mm showed that the CCFL characteristics and the transition from the smooth film (SF) to the rough film (RF) due to flooding near the bottom end were different. On the other hand, δ and f_w for SF were expressed by the same correlation for D = 20 and 40 mm. We discussed the CCFL characteristics and f_w in detail for SF; these items are important for assessment of α and f_i from the dP/dz data in the absence of α data.

Keywords: Countercurrent flow limitation, Flooding, Square top end, Vertical pipe, Wall friction factor

1. Introduction

A normal operation flow in the primary loop of a pressurized water reactor (PWR) consists of single-phase water at about the pressure, P, 15 MPa. It, however, becomes a steam-water two-phase flow under postulated accident conditions such as a small-break loss-of-coolant accident due to depressurization boiling and boiling caused by decay heat in the core. The pressure and water level in the primary loop decrease due to the break flow, and the primary loop pressure is kept at about 7 MPa (which is the operation pressure of the secondary loop in the steam generators with a large heat capacity) for a while, before it decreases again. Therefore, when effects of fluid properties are investigated in an accident analysis, pressures below 7 MPa are important. Countercurrent flows of steam and condensed water appear in the primary loop, and flooding may occur in a small flow region where the steam velocity is high. The objective of this study was to assess the following flow characteristics in vertical pipes under flooding conditions that are important in one-dimensional accident analysis codes: countercurrent flow limitation (CCFL), pressure gradient dP/dz, void fraction α, wall friction factor f_w, and interfacial friction factor f_i.

Many studies on flooding in vertical pipes have been carried out (Wallis, 1969; Bankoff and Lee, 1983). However most of them are on CCFL, so that knowledge on α, f_w and f_i under flooding conditions is limited. Bharathan et al. (1978) measured the liquid film thickness δ and dP/dz, and obtained f_w and f_i under flooding conditions. However f_w were negative under some experimental conditions due to underdetection of δ. Therefore, Bharathan et al. (1979) and Bharathan and Wallis (1983) evaluated f_i from the measured dP/dz by assuming f_w = 0, and proposed an f_i correlation for a rough film (RF) due to flooding at the bottom end. However, they offered little discussion on a smooth film (SF) for flooding at the top end. Goda et al. (2019) measured dP/dz and α in a vertical pipe (diameter of D = 20 and 40 mm; rounded top end (curvature radius of $D/2$) and square bottom end; working fluid of air and water) by using quick closing valves to obtain f_w and f_i for RF. Shimamura et al. (2018) carried out similar experiments, in which dP/dz and α

were measured in a vertical pipe (diameter of D = 20 mm; square top end and rounded bottom end; working fluid of air and water), and obtained f_w and f_i for SF. Murase et al. (2018) pointed out that CCFL characteristics with the square top end can be expressed by the Wallis-type CCFL correlation (Wallis, 1969). The model coefficients (the slope and interception of the CCFL line) of the correlation were constant for a wide range of D (D = 30-250 mm). For a smaller D range (D = 19-25 mm), the interception was smaller than in the former D range, implying different flow characteristics in these D ranges. Hence, data of flow characteristics for SF with $D \geq 30$ mm are desirable for further understanding of flooding behaviour for SF.

In this study, we measured CCFL characteristics, dP/dz and α in a vertical pipe (D = 40 mm; square top end and rounded bottom end; working fluid of air and water), and we obtained f_w and f_i from the measured dP/dz and α. We compared flow characteristics in D = 40 mm with those reported by Shimamura et al. (2018) for D = 20 mm to evaluate effects of D on the flow characteristics for SF. The CCFL characteristics and f_w were analysed in detail since they are important to evaluate α and f_i from the dP/dz data when α data are lacking.

2. Experiments

2.1. Experimental setup and measurement method

Fig. 1 shows the experimental setup. The test section was a vertical pipe of 0.8 m length and 40 mm diameter, and its top and bottom ends were square (i.e. sharp-edged without curvature) and rounded (i.e. smooth; curvature radius of D/2), respectively. Other main components were an upper tank, a lower tank, quick closing valves, and air and water supply systems.

Working fluids were air and water (temperature of 25±5 °C) at atmospheric pressure. Flow rates of air and water were measured by flowmeters (accuracy: ±2.5 % for the full scale). The water level in the upper tank was 0.1 m. CCFL characteristics were also measured for the water level of 0.3 m. The pressure gradient dP/dz was measured for the length of 0.54 m in the test section by using a differential pressure transducer for 50 s with the sampling rate of 1.0 kHz, and the time-averaged value was used. The flow rate, Q_L (m^3/s), of water falling into the lower tank was measured from the increasing rate of the water level in the tank to obtain the superficial liquid velocity J_L (m/s) (= 4 $Q_L/(\pi D^2)$). The uncertainty in J_L estimated at 95 % confidence was ±4.8 %.

The void fraction α (or the liquid volume fraction) was measured by using the quick closing valves. They were synchronized and closed within 1/30 s. The distance between the two quick closing valves was H_{cv} = 0.55 m. The liquid volume fraction $(1-\alpha)_i$ of the ith measurement was obtained by measuring the height H_i of the liquid in the measurement section after closing, i.e. $(1-\alpha)_i = H_i/H_{cv}$. The ensemble-averaged volume fraction $(1-\alpha)_{ave}$ was obtained for measurements repeated n times. We selected n = 60 and used the $(1-\alpha)_{ave}$ value to obtain the time and space averaged $(1-\alpha)$. Uncertainties in α estimated at 95 % confidence were 0.0039, 0.0024 and 0.0024 for the superficial gas velocity J_G = 2.5, 5.1 and 9.3 m/s, respectively.

2.2. Annular flow model

Under flooding conditions in vertical pipes, the flow pattern is an annular flow. Force balance equations for the gas core and the entire cross section in the annular flow model are (Bharathan and Wallis, 1983; Sudo, 1994; Goda et al., 2019; Takaki et al., 2020):

$$\frac{dP}{dz} + \rho_G g + \frac{f_i}{2}\rho_G\left[\frac{J_G}{\alpha} - \frac{J_L}{1-\alpha}\right]^2 \frac{4}{D\sqrt{\alpha}} = 0 \tag{1}$$

and

$$\frac{dP}{dz}+\left[\rho_G \alpha g+\rho_L(1-\alpha)g\right]-\frac{f_w}{2}\rho_L\left(\frac{J_L}{1-\alpha}\right)^2\frac{4}{D}=0 \tag{2}$$

where g is the gravitational acceleration, z is the vertical coordinate, and ρ is the density. The subscripts G and L denote the gas and liquid phases, respectively. Bharathan and Wallis (1983) assumed $J_L/(1-\alpha) << J_G/\alpha$ and simplified Eq. (1). This assumption is however not valid for large α (Goda et al, 2019; Takaki et al., 2020). By measuring dP/dz, α, and CCFL characteristics (J_L for a given J_G), we can obtain f_i and f_w from Eqs. (1) and (2), respectively.

Eqs. (1) and (2) can be rewritten in the following dimensionless forms using the Wallis parameters J_i^*:

$$\left(\frac{dP}{dz}\right)^*+\frac{\rho_G}{\rho_L-\rho_G}+\frac{2f_i}{\alpha^{1/2}}\left[\frac{J_G^*}{\alpha}-\left(\frac{\rho_G}{\rho_L}\right)^{1/2}\frac{J_L^*}{1-\alpha}\right]^2=0 \tag{3}$$

and

$$\left(\frac{dP}{dz}\right)^*+\left[(1-\alpha)+\frac{\rho_G}{\rho_L-\rho_G}\right]-2f_w\left[\frac{J_L^*}{1-\alpha}\right]^2=0 \tag{4}$$

where

$$J_i^*=\left[\frac{\rho_i}{(\rho_L-\rho_G)gLc}\right]^{1/2}J_i \quad (i=G \text{ or } L) \tag{5}$$

here L_C is the characteristic length given by $L_C = D$ and

$$\left(\frac{dP}{dz}\right)^*=\frac{(dP/dz)}{(\rho_L-\rho_G)g}. \tag{6}$$

Since $\rho_G/(\rho_L - \rho_G) << 1$, the absolute value of $(dP/dz)^*$ in Eqs. (3) and (4) nearly equals to the interfacial friction term and the difference between $(1–\alpha)$ and the wall friction term. By eliminating $(dP/dz)^*$ in Eqs. (3) and (4), J_G^* and J_L^* can be related as:

$$(1-\alpha)-2f_w\left[\frac{J_L^*}{1-\alpha}\right]^2-\frac{2f_i}{\alpha^{1/2}}\left[\frac{J_G^*}{\alpha}-\left(\frac{\rho_G}{\rho_L}\right)^{1/2}\frac{J_L^*}{1-\alpha}\right]^2=0. \tag{7}$$

Eq. (7) shows that $(1–\alpha)$ equals the sum of the wall and interfacial friction terms. The CCFL characteristics can be obtained by substituting correlations of f_w and f_i into Eq. (7) and applying the envelope method proposed by Wallis (1969).

2.3. Evaluation of wall and interfacial friction factors

The f_w and f_i can be obtained from the measured values of (dP/dz), J_L and α for a given J_G by using Eqs. (4) and (3) as:

$$f_w=\frac{(dP/dz)^*+(1-\alpha)+\rho_G/(\rho_L-\rho_G)}{2\{J_L^*/(1-\alpha)\}^2}, \tag{8}$$

$$f_i=\frac{-(dP/dz)^*-\rho_G/(\rho_L-\rho_G)}{(2/\alpha^{1/2})\{J_G^*/\alpha-(\rho_L/\rho_G)^{1/2}J_L^*/(1-\alpha)\}^2}. \tag{9}$$

3. Experimental results

3.1. Flow structure

Images of flows in the pipe were taken by using a high-speed video camera with the frame rate of 350 fps. The time-strip flow visualization technique (Borhani et al., 2010) was applied to the images, i.e. the gray values of pixels along the pipe axis were extracted from each image and were rearranged in the horizontal direction.

Fig. 2 shows the time-strip images for D = 20 mm reproduced from the literature (Shimamura et al., 2018). The downward motion of interfacial waves caused by intermittent liquid inflow at the top end and the upward motion of disturbance waves caused by flooding near the bottom end were clearly observed in the time-strip images.

In SF (a), disturbance waves near the bottom end were not observed. In the transition (TR) (b), disturbance waves occurred near the bottom end but they did not reach the upper tank. In RF (c), disturbance waves reached the upper tank and J_L was zero (see the CCFL characteristics later in Fig. 5 and Sec. 3.3). SF, TR and RF are for classification of flow structure shown by Bharathan and Wallis (1983), and the gas-liquid interface in SF is not actually smooth due to interfacial waves.

Fig. 3 shows the time-strip images for $D = 40$ mm. In SF (a), the downward motion of interfacial waves caused by intermittent liquid inflow at the top end was observed. In TR (b), disturbance waves occurred near the bottom end. Some of the disturbance waves reached the upper tank but others did not reach there. Transition from TR to RF did not take place even with increasing J_G within the present experimental range, so that the J_G range for TR was wider than for $D = 20$ mm. The flow regime at the largest J_G^* could not be clearly distinguished as TR or RF from the visual observation. In the following this data point will be shown as TR.

3.2. Pressure gradient and liquid volume fraction

Fig. 4 shows the measured $(dP/dz)^*$ and $(1-\alpha)$. As shown in Figs. 2 and 3, flooding occurred at the top end in the region of low J_G^* (i.e. SF), at the top end and near the bottom end simultaneously in the region of medium J_G^* (i.e. TR), and near the bottom end in the region of high J_G^* (i.e. RF). $-(dP/dz)^*$ were relatively small for SF due to the thin liquid film and they were relatively large for RF due to the thick liquid film. $(1-\alpha)$ decreased in the regions of SF and RF with increasing J_G^*, whereas $(1-\alpha)$ for TR increased with increasing J_G^* due to increase in the height of the disturbance wave region.

The difference between $(1-\alpha)$ and $-(dP/dz)^*$ is nearly equal to the term of f_w, and $-(dP/dz)^*$ is close to the term of f_i as shown in Eqs. (4) and (3), respectively. The f_w term was large and the f_i term was small in SF. On the other hand, the f_w term was small and the f_i term was large in RF. In RF for D = 20 mm, J_L = 0. The f_w term became very small at large J_G^* for D = 40 mm.

The different behavior between D = 20 mm and 40 mm was observed in TR. For D = 40 mm, TR appeared at low J_G^* and its region was wide. In the experiment with the rounded top end and square bottom end reported by Goda et al. (2019), the f_w term for RF was relatively large for D = 20 mm similar to that in Fig. 4 but was small for D = 40 mm similar to that at high J_G^* in Fig. 4. Evaluation of change from TR to RF in detail remains as future work.

3.3. CCFL characteristics

In accident analysis codes, the following Wallis CCFL correlation (Wallis, 1969) is widely used to compute J_L for a given J_G under flooding conditions, because uncertainty of J_L computed with Eq. (7) is generally large.

$$J_G^{*1/2} + m\,J_L^{*1/2} = C \tag{10}$$

Here C and m are empirical constants. Bankoff et al. (1981) proposed the characteristic length L_C in Eq. (5) expressed by:

$$L_C = D^{(1-\beta)} L^{\beta} \ \ (0 \le \beta \le 1),\ \ L = \left[\frac{\sigma}{(\rho_L - \rho_G)g}\right]^{1/2}, \tag{11}$$

where L is the Laplace length and σ is the surface tension. The Wallis parameter J_i^* defined by Eq. (5) can be converted to the Kutateladze parameter K_i^* by using the dimensionless diameter D^* (= D/L) as follows:

$$K_i^* = D^{*1/2} J_i^* \ (i = G \text{ or } L). \tag{12}$$

In Eq. (11), β = 0 for flooding at the bottom end, i.e. CCFL-L (Kusunoki et al., 2016), and β = about 0.5 for flooding inside vertical pipes, i.e. CCFL-P (Yamamoto et al., 2016).

For CCFL-P in large pipes, $\beta = 1$ and $C_K = 1.79$ with the Kutateladze parameters in Eq. (10) (Wallis and Kuo, 1976), and Yamamoto et al. (2016) proposed the CCFL-P correlation as:

$$K_G^{*1/2} + 0.90\, K_L^{*1/2} = \min\left[(1.2 \pm 0.07)\, D^{*1/8}, 1.79\right] \text{ for } 6.6 \le D^* \le 38 \tag{13}$$

For flooding at the top end, i.e. CCFL-U, CCFL could be expressed by the Kutateladze parameters ($\beta = 1$) for $D \ge 30$ mm (Murase et al., 2018).

$$K_G^{*1/2} + 0.97\, K_L^{*1/2} = 1.53 \pm 0.11 \text{ for } D \ge 30 \text{ mm} \tag{14}$$

Fig. 5 shows CCFL characteristics expressed by (a) the Wallis parameters and (b) the Kutateladze parameters. The CCFL curve gives the relationship between the gas and liquid flow rates (i.e. J_G and J_L) under flooding conditions. $J_L^{*1/2}$ for D = 40 mm was smaller than that for D = 20 mm and $K_L^{*1/2}$ for D = 40 mm was larger than that for D = 20 mm. This shows that the effects of D on the CCFL characteristics cannot be expressed by the Wallis parameters nor the Kutateladze parameters. The data for D = 40 mm were within the uncertainty of ± 0.11 of Eq. (14) for flooding at the top end and $D \ge 30$ mm. The data for D = 20 mm could not be expressed by the Kutateladze parameters since D was not within the applicable range of Eq. (14). The C_K values for D = 19-25 mm were smaller than those for $D \ge 30$ mm (Murase et al., 2018).

3.4. Wall friction factor

$(dP/dz)^*$ and α data are required to obtain f_w from Eq. (4). However, α data under flooding conditions are limited, and no reliable f_w for SF has been obtained. Therefore, the following f_w correlation for single-phase flows is widely used (Sudo, 1994; Takaki et al., 2020):

$$f_w = \max\left(\frac{16}{\mathrm{Re}_L}, \frac{0.079}{\mathrm{Re}_L^{0.25}}\right), \tag{15}$$

where Re_L is the liquid Reynolds number defined by $Re_L = J_L D/\nu_L$ and ν is the kinematic viscosity. Takaki et al. (2020) proposed a f_w correlation (f_w = $2.68/Re_L^{0.70}$) for the transition region between laminar and turbulent flows by using $(dP/dz)^*$ and α data (Shimamura et al., 2018) under flooding at the top end. Takaki et al. (2020) speculated that the combination of Eq. (15) and $f_w = 2.68/Re_L^{0.70}$ would be appropriate, i.e.

$$f_w = \max\left(\frac{16}{\mathrm{Re}_L}, \frac{2.68}{\mathrm{Re}_L^{0.70}}, \frac{0.079}{\mathrm{Re}_L^{0.25}}\right). \tag{16}$$

Fig. 6 shows f_w plotted against Re_L. The f_w data of SF for D = 20 mm were expressed well by Eq. (16). The difference between $(1-\alpha)$ for D = 20 mm (Shimamura et al., 2018) and $(1-\alpha)$ computed with Eqs. (4) and (16) was less than ±0.005 for SF. The f_w data of SF for D = 40 mm were expressed by the prediction of Hewitt's analysis (unpublished work, 1967; reported by Wallis (1969)). Averaging f_w in Eq. (16) and Hewitt's analysis may give good predictions both for D = 20 and 40 mm. The f_w data of TR for D = 40 mm were expressed well by the correlation for RF proposed by Goda et al. (2019).

3.5. Liquid film thickness

In the annular flow model, the relationship between the void fraction α and the liquid film thickness δ is expressed by:

$$\alpha = \left(1 - \frac{2\delta}{D}\right)^2 \quad \text{or} \quad \frac{\delta}{D} = \frac{1-\alpha^{1/2}}{2} \tag{17}$$

For SF under the flooding condition at the top end, Nusselt's equation (Nusselt, 1916) for free-falling films is widely used for δ in laminar flows. Imura et al. (1977) used Feind's empirical correlation (Feind, 1960) for turbulent flows to evaluate α in vertical pipes under flooding conditions. The combination of Nusselt's equation and Feind's empirical correlation is given by:

$$\frac{\delta}{L_v} = \max\left[\left(\frac{3\mathrm{Re}_L}{4}\right)^{1/3}, 0.266\,\mathrm{Re}_L^{1/2}\right], \tag{18}$$

where $L_v = (\nu_L^2/g)^{1/3}$. In our previous study (Takaki et al., 2020), we assessed α by using Eqs. (4) and (16) and $(dP/dz)^*$ and CCFL data in an air-water system (D = 50.8 mm) reported by Bharathan et al. (1978) and those in a steam-water system (D = 20 mm) at P = 0.6-4.1 MPa reported by Ilyukhin et al. (1988), and we proposed the following δ correlation for turbulent flows including the α data in an air-water system reported by Shimamura et al. (2018):

$$\frac{\delta}{L_v} = \max\left[\left(\frac{3\mathrm{Re}_L}{4}\right)^{1/3}, 0.091\,\mathrm{Re}_L^{0.64}\right]. \tag{19}$$

Fig. 7 shows δ, which was obtained from Eq. (17) and $(1-\alpha)$ data shown in Fig. 4. The δ data for SF were relatively well expressed by Eq. (19). On the other hand, the δ data were larger than Eq. (19) in the transition region between the laminar and turbulent flows, which indicates a new correlation for the transition region is desirable. In TR, δ was thicker than the value predicted by Eq. (19) for SF due to the disturbance wave caused near the bottom end (see Figs. 2 and 3).

3.6. Interfacial friction factor

The f_i can be computed by using Eqs. (7), (14), (16) and (19). In accident analysis codes, however, a correlation for f_i is sometimes used. Bharathan and Wallis (1983) proposed a f_i correlation for RF:

$$f_i = 0.005 + A\left(\frac{\delta}{L}\right)^B,\ \log_{10}A = -0.56 + \frac{9.07}{D^*},\ B = 1.63 + \frac{4.74}{D^*}. \tag{20}$$

Fig. 8 shows f_i against J_G^*. With increasing J_G^*, the f_i data decreased in SF, increased in TR, and decreased again. This trend was clearly seen for D = 20 mm and the f_i data decreased again in RF. For D = 40 mm, however, the f_i data increased and changed to decrease at J_G^* = about 0.3 in TR with increasing J_G^*. This trend was caused by the change of $(1-\alpha)+(dP/dz)^*$ at J_G^* = about 0.3 in TR (see Fig. 4). Eq. (20) is for RF, but it agreed with the f_i data for D = 20 mm except for a low J_G^* region. Eq. (20) underestimated f_i for D = 40 mm.

Sudo (1994) obtained f_i for SF by fitting J_L^* computed by applying the envelope method (Wallis, 1969) to the CCFL data reported by Richter (1981), and improved Eq. (20). Takaki et al. (2020) however showed that the f_i correlation of Sudo (1994) overestimated f_i for the data reported by Shimamura et al. (2018), because the envelope method overestimated J_L^* and a large f_i value should be given to fit the computed J_L^* to the measured J_L^*.

Goda et al. (2019) proposed an f_i correlation for RF based on data for D = 20 and 40 mm as a function of J_G^*. Sano et al. (2020) proposed an f_i correlation for RF based on data for a wide range of D (D = 6.6-152 mm) as a function of K_G^*. For SF, however, the f_i data have not been correlated, and Fig. 8 showed that an f_i correlation should be developed for SF.

4. Discussion

4.1. CCFL characteristics

CCFL for flooding at the top end (CCFL-U) can be expressed by Eq. (14) for $D \geq$ 30 mm (Murase et al., 2018). However, effects of fluid properties were not confirmed, and the C_K values for D = 19-25 mm were smaller than those for $D \geq$ 30 mm. Fig. 9 shows CCFL characteristics for D = 20 mm reported by Shimamura et al. (2018), Ilyukhin et al. (1988), and Matsumura and Kaminaga (2012). They used a vertical pipe with a top shape similar to that in Fig. 1, with a protruding end into the upper tank, and with a flat plate in the upper tank for visual observation, respectively. The shape difference at the top end did not affect CCFL characteristics. From these data, therefore, we derived the following CCFL correlation for D = 20 mm by using the least square method:

$$J_G^{*1/2} + 1.07\, J_L^{*1/2} = 0.84 \pm 0.052.\ (D = 20\text{ mm}) \tag{21}$$

In Eq. (21), the uncertainty of ±0.052 includes 95 % of 87 data points.

Fig. 10 compares Eq. (21) with CCFL data for D = 19-25 mm reported by Richter (1981) and Bharathan et al. (1979). The major difference between the experiments reported by Richter (1981) and Bharathan et al. (1979) was the water level h in the upper tank, i.e. the gas phase continued from the pipe to the atmosphere (i.e. low h) and the gas phase was covered by the mixture level (i.e. mid-level), respectively. The data with the low h were within the uncertainty of Eq. (21) at large J_G^* but were outside that uncertainty at small J_G^*. The data for D = 25 mm and the mid-level similar to the data shown in Fig. 9 were outside the uncertainties of both Eqs. (21) and (14) for $D \geq 30$ mm.

Doi et al. (2012) showed that the constant C_K and slope m increased with increasing h in air-water experiments with D = 30 mm and h = 0.1-0.6 m. Therefore, we carried out an additional experiment for D = 40 mm and h = 0.3 m. Fig. 11 compares the CCFL data with h = 0.1 m and 0.3 m. In the case of h = 0.3 m, C_K = 1.48 and m = 1.14 were larger than C_K = 1.43 and m = 0.90 for h = 0.1 m; this trend was similar to the data for D = 30 mm by Doi et al. (2012).

Ilyukhin et al. (1999) referred to their earlier work (Ilyukhin et al., 1988) and reported a CCFL correlation based on their previously obtained data with the square top and bottom ends, D = 20-100 mm, the system pressure of P = 1-8 MPa, and high h (its actual value was not reported) as:

$$\frac{K_G^{*1/2}}{D^{*1/8}} + 1.25\frac{K_L^{*1/2}}{D^{*1/8}} = 1.5\left(\frac{\rho_G}{\rho_L}\right)^{0.05} \tag{22}$$

where $\beta = 0.5$ in Eq. (11). Eq. (22) is a correlation for flooding at the top and bottom ends. Yamamoto et al. (2016) previously proposed $\beta = 0$ for flooding at the bottom end and $\beta = 1$ for flooding at the top end. Ilyukhin et al. (1999) reported CCFL data for $D = 30$ and 40 mm and $P = 0.3$-1.6 MPa on the $K_G^{*1/2}/D^{*1/8}$-$K_L^{*1/2}/D^{*1/8}$ plane, but the values of P were not given for each datum. Therefore, we evaluated K_G^* and K_L^* for $D = 30$ and 40 mm with the fluid properties at $P = 1.0$ MPa, which are shown in Fig. 11. The CCFL data for $D = 30$ and 40 mm agreed with each other better on the $K_G^{*1/2}$-$K_L^{*1/2}$ plane (i.e. $\beta = 1$ in Eq. (11)) than on the $K_G^{*1/2}/D^{*1/8}$-$K_L^{*1/2}/D^{*1/8}$ plane (which is not shown here). Our data for $D = 40$ mm, $h = 0.3$ m and $P = 0.1$ MPa in the air-water system agreed with the data of Ilyukhin et al. (1999). This means that the effects of the fluid properties on the CCFL characteristics were relatively small in the expression with the Kutateladze parameters (i.e. $\beta = 1$ in Eq. (11)). On the other hand, Ilyukhin et al. (1999) reported that C_K for $P =$ 1-8 MPa was 1.1 times larger than that for 0.3-1.6 MPa. The C_K for $P = 1$-8 MPa, which was 1.1 times the average value for $D = 30$ and 40 mm, is shown in Fig. 11. The C_K values for $P = 1$-8 MPa were within the uncertainty range of Eq. (14).

4.2. Wall friction factor

A correlation for f_w is required to obtain α from the pressure gradient data and Eq. (4). Therefore, we re-evaluated Eq. (16) for SF using the f_w data for $D = 20$ and 40 mm. Fig. 12 shows the f_w data. From the data for $Re_L > 430$, a correlation for the transition region between laminar and turbulent flows was derived by using the least square method, and Eq. (16) was modified to:

$$f_w = \max\left(\frac{16}{\mathrm{Re}_L}, \frac{0.70}{\mathrm{Re}_L^{0.50}}, \frac{0.079}{\mathrm{Re}_L^{0.25}}\right). \tag{23}$$

Eq. (23) is very close to the prediction of Hewitt's analysis (unpublished work, 1967; reported by Wallis (1969)). One data point for $D = 40$ mm was far from the line drawn using Eq. (23). Though its flow regime was classified as SF from the visual observation, the characteristic of f_w was similar to that in TR rather than SF (see Fig. 6).

4.3. Void fraction and interfacial friction factor

The α and f_i can be obtained from the CCFL characteristics and dP/dz by using Eqs. (3), (4) and (23). In this case, however, the uncertainty for the obtained α tends to be relatively large due to the difference between Eq. (23) and the data shown in Fig. 12. Fig. 13 compares $(1–\alpha)$ computed from dP/dz data and Eq. (23) with the measured $(1–\alpha)$. The uncertainty of dP/dz data and the difference between Eq. (23) and f_w data gave the uncertainty of ±0.008 for $(1–\alpha)$ in the range of $(1–\alpha)$ = 0.05-0.13. The difference between the computed and measured α shown in Fig. 13 propagated to the obtained f_i even though the effect of α on f_i computed by Eq. (3) was not large. Correlations of α for SF are often expressed in terms of δ like Eq. (18). The δ data were relatively well expressed by Eq. (19) as shown in Fig. 7. However, the δ data clearly differed from Eq. (19) in the transition region between laminar and turbulent flows. Available correlations for f_i like Eq. (20) did not agree with the f_i data especially for D = 40 mm as shown in Fig. 8. An improvement of correlations for δ and f_i remains as future work.

5. Conclusions

In this study, we measured the void fraction α, pressure gradient dP/dz, and CCFL (falling liquid velocity J_L for a given gas velocity J_G) in a vertical pipe of diameter D = 40 mm, with the square top end and working fluid of air and water under flooding conditions. The liquid film thickness δ, wall friction factor f_w and interfacial friction factor f_i were evaluated based on the annular flow model. The measured data were compared with those for D = 20 mm obtained in our previous study (Shimamura et al., 2018). Conclusions obtained are as follows.

(1) CCFL characteristics for $D = 40$ mm were within the uncertainty of our previously proposed correlation with the Kutateladze parameters (K_G^* and K_L^*) for $D \geq 30$ mm (Murase et al., 2018). CCFL characteristics for $D = 20$ mm were expressed by the proposed empirical equation, Eq. (21), with the Wallis parameters (J_G^* and J_L^*) for the air-water system at the pressure of $P = 0.1$ MPa and the steam-water system at $P = 0.6$-4.1 MPa reported by Ilyukhin et al. (1988). The CCFL constant C_K and slope m for $D = 40$ mm increased with increasing water level h in the upper tank from $h = 0.1$ m to $h = 0.3$ m. The CCFL characteristics for $D = 40$ mm and $h = 0.3$ m agreed with the steam-water data for $D = 30$ and 40 mm, $P = 0.3$-1.6 MPa, and high h by Ilyukhin et al. (1999) on the K_G^*-K_L^* plane. This means that effects of fluid properties on CCFL characteristics are not large.

(2) The wall friction factor f_w for smooth films caused by flooding at the top end was expressed by the standard correlation, Eq. (15), but it was larger than Eq. (15) in the transition region between laminar and turbulent flows, hence an empirical equation, Eq. (23), was proposed to better describe the transition region. The prediction of $(1–\alpha)$ from dP/dz data and Eq. (23) gave the uncertainty of ± 0.008 in the range of $(1–\alpha) = 0.05$-0.13.

(3) The liquid film thickness δ for SF was expressed by our previously proposed empirical equation (Takaki et al., 2020), Eq. (19), but that thickness was larger than the thickness calculated here with Eq. (19) in the transition region between laminar and turbulent flows.

Nomenclature

C	CCFL constant [-]
D	pipe diameter [m]

D^* dimensionless pipe diameter [-]

f_i interfacial friction factor [-]

f_w wall friction factor [-]

g gravitational acceleration [m/s^2]

H length of test section [-]

h water level [m]

J superficial velocity [m/s]

J^* Wallis parameter [-]

K^* Kutateladze parameter [-]

L Laplace length [m]

L_C characteristic length [m]

L_v length [m]

m slope of CCFL characteristics [-]

P pressure [Pa]

Re Reynolds number [-]

z axial coordinate [m]

Greek letters

α void fraction [-]

β exponent in Eq. (11) [-]

δ liquid film thickness [m]

ν kinematic viscosity [m^2/s]

ρ density [kg/m^3]

σ surface tension [N/m]

Subscripts

G gas phase

i G or L

in inlet

K Kutateladze parameter

L liquid phase

Superscript

* dimensionless form

Acknowledgement

The authors would like to express their thanks to Mr. Takeyuki Shimamura (Graduate School of Engineering, Kobe University) for his assistance in the experiments.

References

Bankoff, S.G., Lee, S.C., 1983. A critical review of the flooding literature, NUREG/CR-3060, U.S. Nuclear Regulatory Commission, Washington D.C.

Bankoff, S.G., Tankin, R.S., Yuen, M.C., Hsieh, C.L., 1981. Countercurrent flow of air/water and steam/water through a horizontal perforated plate, Int. J. Heat Mass Transfer 24 (8), 1381-1395.

Bharathan, D., Wallis, G.B., 1983. Air-water countercurrent annular flow, Int. J. Multiphase Flow 9(4), 349-366.

Bharathan, D., Wallis, G.B., Richter, H.J., 1978. Air-water countercurrent annular flow in vertical tubes, EPRI NP-786, Electric Power Research Institute, Palo Alto, California.

Bharathan, D., Wallis, G.B., Richter, H.J., 1979. Air-water countercurrent annular flow, EPRI NP-1165, Electric Power Research Institute, Palo Alto, California.

Borhani, N., Agostini, B., Thome, J.R., 2010. A novel time strip flow visualization technique for investigation of intermittent dewetting and dryout in elongated bubbly flow in a microchannel evaporator, Int. J. Heat Mass Transfer 53, 4809-4818.

Doi, T., Futatsugi, T., Murase, M., Hayashi, K., Hosokawa, S., Tomiyama, A., 2012. Countercurrent flow limitation at the junction between the surge line and the pressurizer of a PWR, Sci. Technol. Nucl. Installations 2012, Article ID 754724, 9 pages.

Feind, K., 1960. Shrömungsuntersuchungen bei gegensttom von rieselfilmen und gas in lotrechten rohren, VDI-Forschungsheft 481, 35 pages.

Goda, R., Hayashi, K., Murase, M., Hosokawa, S., Tomiyama, A., 2019. Experimental study on interfacial and wall friction factors under counter-current flow limitation in vertical pipes with sharp-edged lower ends, Nucl. Eng. Des. 353, ID 110223.

Goda, R., Shimamura, T., Hayashi, K., Hosokawa, S., Murase, M., Tomiyama, A., 2019b. Interfacial and wall friction factors for gas-liquid counter-current flow in vertical pipes, Proc. of Japanese Symposium on Multiphase Flow 2019, D314, Fukuoka, Japan. (in Japanese)

Imura, H., Kusuda, H., Funatsu, S., 1977. Flooding velocity in a counter-current annular two-phase flow, Chemical Eng. Sci. 32(1), 79-83.

Ilyukhin, Yu.N., Balunov, B.F., Smirnov, E.L., Gotovskii, M.A., 1988. Hydrodynamic characteristics of annular counter flows in vertical channels, Teplofiz. Vys. Temp. 26 (5), 923-931. (in Russian)

Ilyukhin, Yu. N., Svetlov, S.V., Alekseev, S.B., Kukhtevich, V.O., Sidorov, V.G., 1999. The hydrodynamic characteristics of the process of "flooding" under conditions of countercurrent flow of steam and water in vertical tubes, High Temp. 37 (3), 463-469.

Kusunoki, T., Doi, T., Fujii, Y., Tsuji, T., Murase, M., Tomiyama, A., 2014. Air-water tests on counter-current flow limitation at lower end of vertical pipes simulating lower part of steam generator U-tube, Japanese J. Multiphase Flow 28(1), 62-70. (in Japanese)

Kusunoki, T., Nozue, T., Hayashi, K., Hosokawa, S., Tomiyama, A., Murase, M., Condensation experiments for counter-current flow limitation in an inverted U-tube, 2016. J. Nucl. Sci. Technol. 53(4), 486-495.

Matsumura, K., Kaminaga, F., 2012. Experimental investigation of rising gas bubble characteristics from a vertical tube under CCFL condition, Sci. Technol. Nucl. Installations 2012, Article ID 785157, 15 pages.

Murase, M., Nishida, K., Torige, T., Takaki, T., Goda, R., Tomiyama, A., 2018. Effects of diameters on countercurrent flow limitation at a square top end in vertical pipes, Sci. Technol. Nucl. Installations 2018, Article ID 1426718, 11 pages.

Nusselt, W., 1916. Die oberflachenkondensation des wasserdampfes, Z. Ver. Deut. Ing. 60(541), 569.

Richter, H.J., 1981. Flooding in tubes and annuli, Int. J. Multiphase Flow 7 (6), 647-658.

Sano, N., Takaki, T., Nishida, K., Murase, M., Goda, R., Tomiyama, A., 2020. Interfacial friction factors in vertical circular pipes under flooding conditions at the bottom end, Japanese J. Multiphase Flow 34(1), 82-92. (in Japanese)

Shimamura, T., Goda, R., Hayashi, K., Hosokawa, S., Tomiyama, A., Murase, M., Nishida, K., 2018. Interfacial and wall frictions under flooding conditions in a vertical pipe with the sharp-edged upper end, Proc. of Japanese Symposium on Multiphase Flow 2018, D212, Sendai, Japan. (in Japanese)

Sudo, Y., 1994. Limitation of falling water in countercurrent two-phase flow in vertical circular tubes, Trans. of the JSME 60(575), 2566-2572. (in Japanese)

Takaki, T, Murase, M., Nishida, K., Goda, R., Shimamura, T., Tomiyama, A., 2020. Liquid film thickness in vertical circular pipes under flooding conditions at the top end, Nuclear Technology 206(3), 389-400.

Wallis, G.B., 1969. One-dimensional Two-phase Flow, McGraw Hill, New York, 336-345.

Wallis, B.G., Kuo, J.T., 1976. The behavior of gas-liquid interfaces in vertical tubes, Int. J. Multiphase Flow 2, 521-536.

Yamamoto, Y., Murase, M., Hayashi, K., Hosokawa, S., Tomiyama, A., 2016. Counter-current flow limitation inside vertical pipes, Japanese J. Multiphase Flow 30 (4), 392-401. (in Japanese)

Figure 1

Experimental setup.

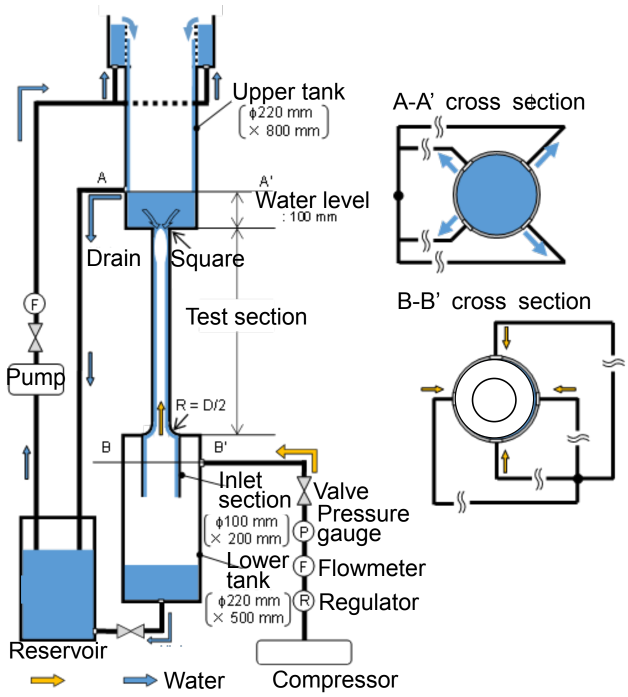

Figure 2

Time-strip images (D = 20 mm) obtained by Shimamura et al. (2018).

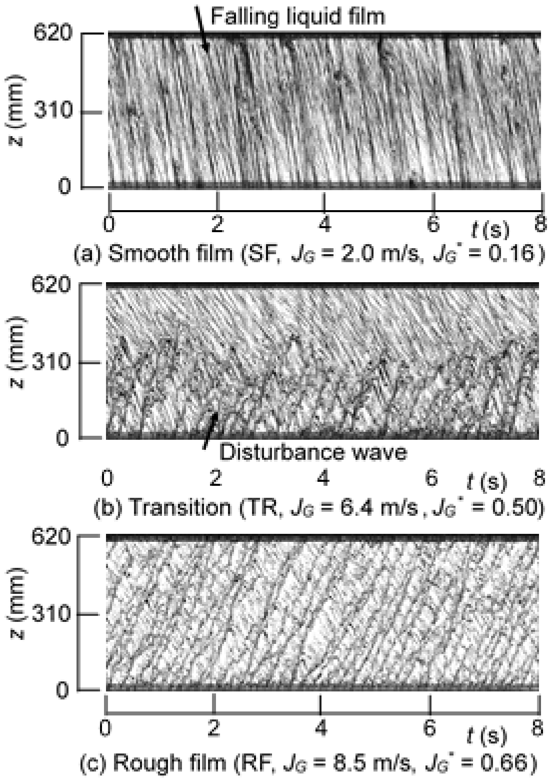

Figure 3

Time-strip images (D = 40 mm).

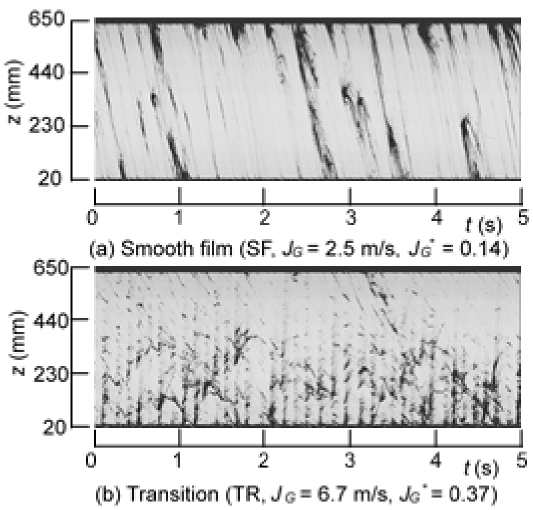

Figure 4

Dimensionless pressure gradient $(dP/dz)^*$ and liquid volume fraction $(1-\alpha)$. (a) D = 20 mm, (b) D = 40 mm.

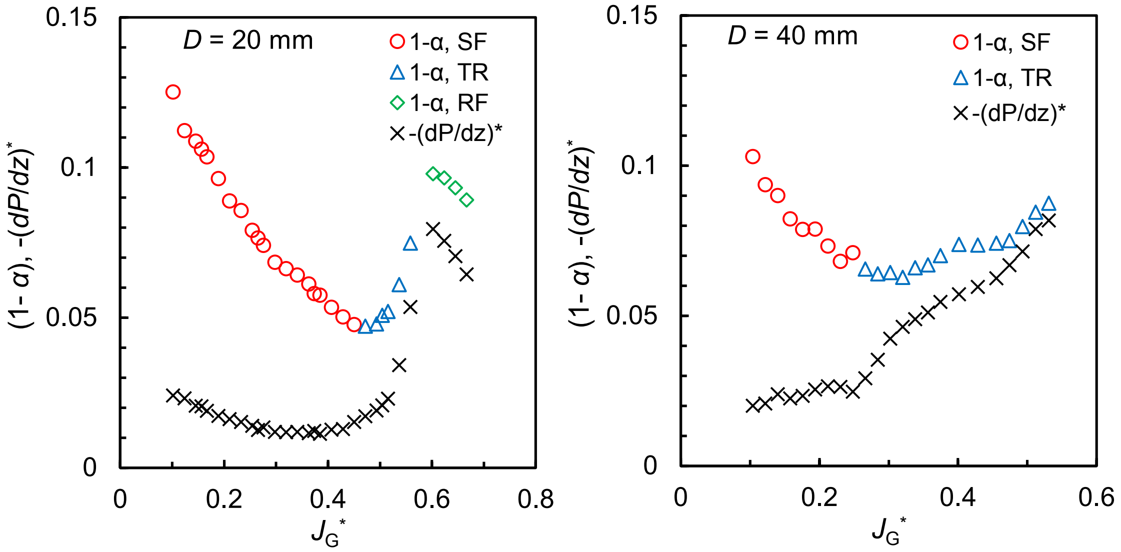

(a) (b)

Figure 5

CCFL characteristics expressed by (a) the Wallis parameters and (b) the Kutateladze parameters.

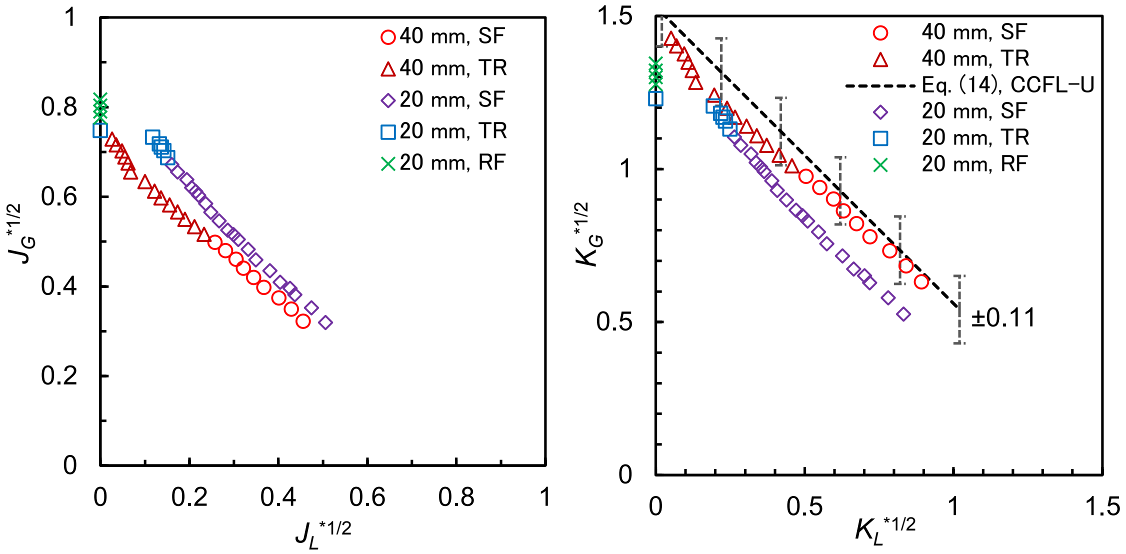

(a) (b)

Figure 6

Wall friction factor f_w. The dashed line represents unpublished data of Hewitt reported by Wallis (1969).

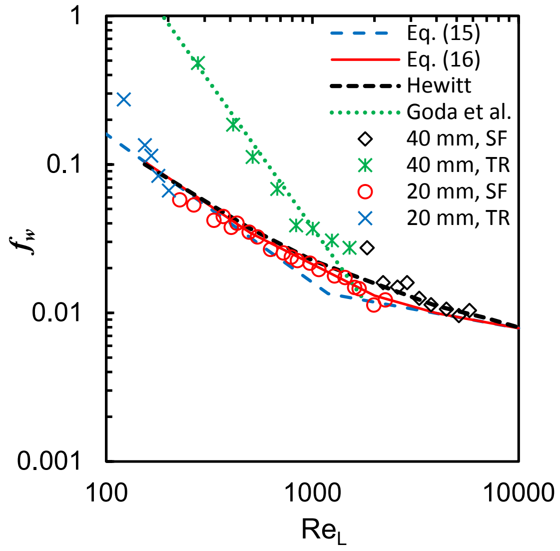

Figure 7

Liquid film thickness δ.

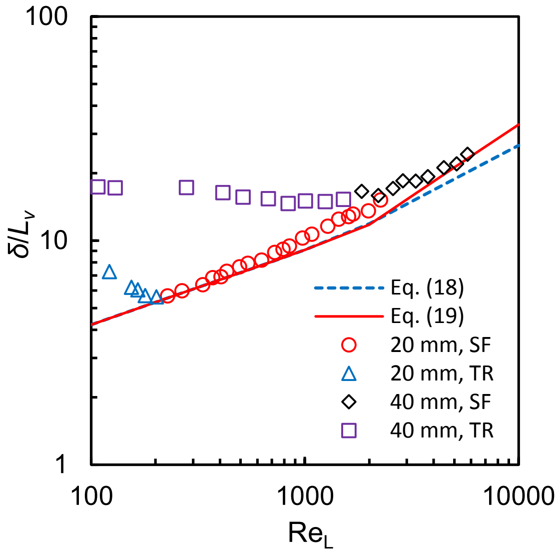

Figure 8

Interfacial friction factor f_i.

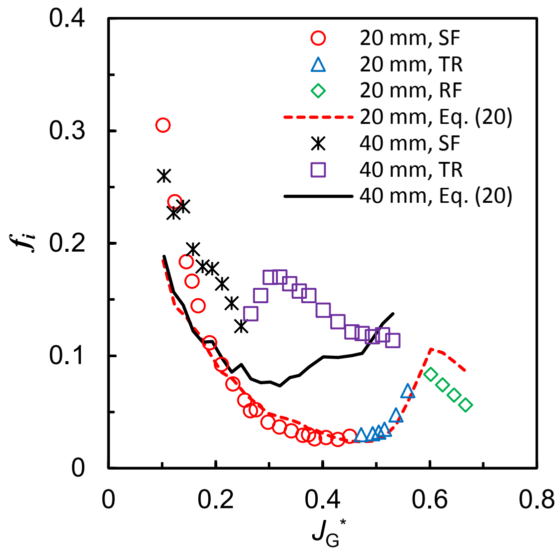

Figure 9

CCFL characteristics with D = 20 mm (0.1 MPa, air-water; 0.6-4.1 MPa, steam-water).

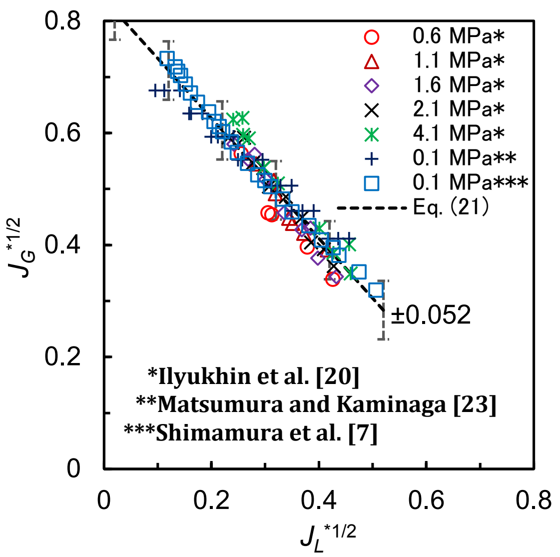

Figure 10

CCFL characteristics with D = 19 and 25 mm and air-water at 0.1 MPa.

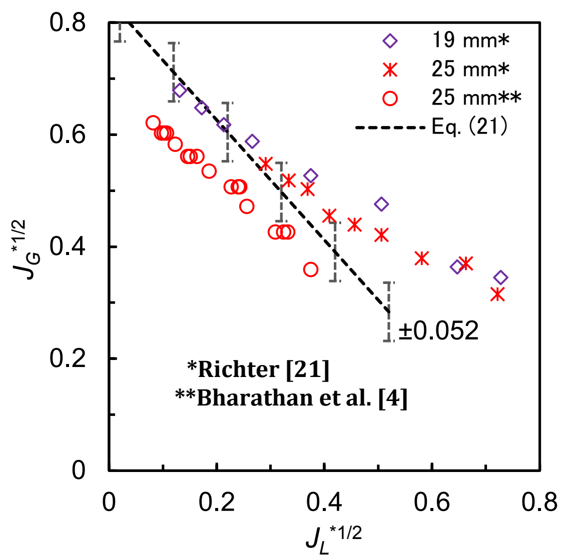

Figure 11

Effects of the water level in the upper tank h and system pressure P on CCFL characteristics with D = 30 and 40 mm (*Ilyukhin et al. (1999)).

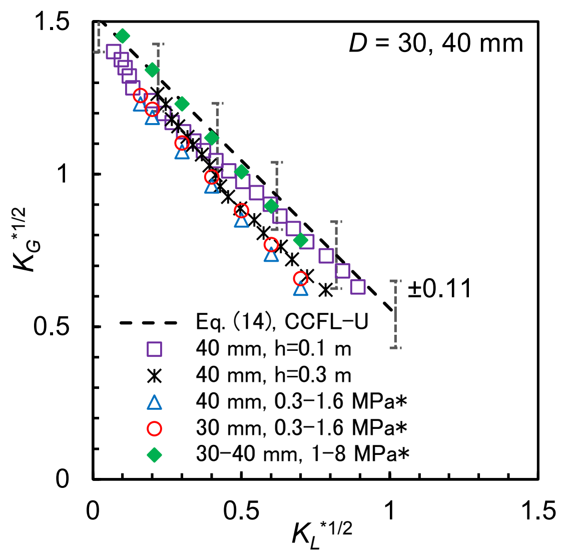

Figure 12

Wall friction factor for smooth films. The dashed line marked Hewitt represents unpublished Hewitt's analysis reported by Wallis (1969).

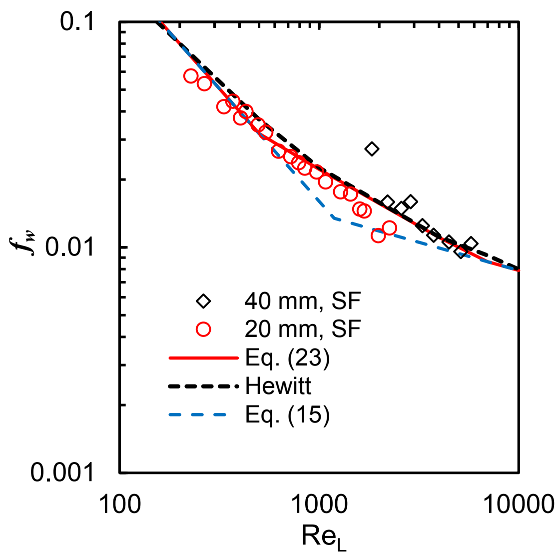

Figure 13

Comparison of (1–α) computed from dP/dz data and Eq. (23) with the measured (1–α).